

Czech Technical University in Prague
Faculty of Nuclear Sciences and Physical Engineering
Department of Physics



Bachelor thesis
Lukáš Sedlák

Prague 2011

Czech Technical University in Prague
Faculty of Nuclear Sciences and Physical Engineering
Department of Physics



Development of optical diagnostics for the COMPASS tokamak

Bachelor thesis

Author: Lukáš Sedlák
Leader: Ing. Diana Naydenkova
Academic year: 2010/2011

Statement

I proclaim that I elaborated my bachelor thesis alone and I used basics listed in Bibliography only. (literature, projects, software, etc.)

I have not any reason against the thesis usage *a posteriori* § 60 law number 121/2000 Sb., author's law, laws dependent on author's law and changes some laws (author's law).

Prohlášení

Prohlašuji, že jsem svou bakalářskou práci vypracoval samostatně a použil jsem pouze podklady (literaturu, projekty, SW, atd.) uvedené v příloženém seznamu.

Nemám závažný důvod proti užití tohoto školního díla ve smyslu § 60 Zákona č.121/2000 Sb., o právu autorském, o právech souvisejících s právem autorským a o změně některých zákonů (autorský zákon).

In Prague at / V Praze dne _____

Lukáš Sedlák

Abstract Main goals of COMPASS tokamak operation are to study: role of multi-scale mechanism in the L-H transition; L-H power threshold and ELM control techniques; hysteresis L-H versus H-L transition; role of atomic physics mechanisms; turbulent structures and intermittency; edge localized modes. Theory developing and modelling of edge turbulence.

New visible light diagnostics consists of a multichannel diagnostics and few spectrometers. Testing of the tools is aim of the paper. Test results was published in article [2].

Keywords: multichannel diagnostics, spectrometers, photomultiplier tubes, visible spectroscopy, tokamak, COMPASS

Abstrakt Hlavním cílem tokamaku COMPASS je studium: víceškálového mechanismu v L-H přechodu; limitu L-H výkonu a způsoby regulace ELMů; zpoždování L-H přechodu vůči H-L přechodu; mechanismů atomové fyziky; neuspořádaných struktur a nesouvislostí; ELMů. Vývoj a modelování okrajů turbulencí.

Nová diagnostika viditelného záření se skládá z vícekanálové diagnostiky a z několika spektrometrů. Cílem této práce je testování této diagnostiky viditelného záření. Získané poznatky budou také zveřejněny v [2].

Klíčová slova: vícekanálová diagnostika, spektrometr, fotonásobič, spektrometrie viditelného záření, tokamak, COMPASS

Acknowledgement I would like to thank to many people, who supported me. First of all, I would like to thank my mentor Ing. Diana Naydenkova, who helped me with gathering knowledge about the plasma spectroscopy. Also many other people from AVČR helped me to understand the tokamak physics. Next, I would like to mention all people of my *alma mater*, who guided me through the deeps of physics. Finally I would like to thank to my family and friends for various support during my study and writing.

Contents

Statement	i
Abstract	ii
Acknowledgement	iii
Contents	iv
1 Introduction	1
2 Optical diagnostic	2
2.1 Plasma parameters we are interested in	2
2.2 Diagnostic structure	4
3 The multichannel diagnostic	6
3.1 Description of the multichannel diagnostic	6
3.2 Amplifier's "time constant" measurements	10
3.3 Detector sensitivity tests	11
3.4 Alignment	13
4 Spectrometers	16
4.1 Description of the spectrometers	16
4.2 Spectrometer calibration	17
5 Photomultiplier	20
5.1 Photomultiplier tube description	20
5.2 Photomultiplier tubes tests	22
6 FLYCHK simulation	24
6.1 Simulation theory	24
6.2 Simulation execution	25
7 Conclusion	27
Bibliography	28

Chapter 1

Introduction

Energy consumption increases during growth of our civilization and rise of new technologies. It is natural to secure future generations and explore all possible ways of energy production. Today's issues are also painful for our society and shame us. Sufficient energy source could provide enough energy for water cleaners in Africa and make it prosper instead of starve as today. Recently with rise of Asia nations energy hunger is much bigger again. Limited and exhaustible resources of coal and oil can not cover energy need for long. Renewable energy sources have low power and are nature-dependent. Nuclear energetics rise once more again. New nuclear power plants will be build. However nuclear energetics has to deal with several problems. At first, nuclear power plants are not allowed in every country. Secondly, strong risk for environment still remains. The most commonly-known problem with nuclear waste does not need comment.

Since discovering fusion reaction in the Sun, fusion potential as energy source had been proved. Part of the mass is converted to neutron energy during the fusion reaction $D_1^2 + T_1^3 \rightarrow He_2^4 + n_0^1$. Fusion energy profit is much bigger than fission one as proved by theory. However, technological difference between fission power plant and fusion power station is essential. Since fission fuel manipulation is much easier, hydrogen plasma manipulation is sophisticated. Fusion radiation is completely at different level, which has higher demands on materials. Fusion research continue for fifty years, fusion theory had been based and several tokamaks had been built. However, many technological questions stay unanswered.

ITER tokamak will be first experimental fusion power plant. COMPASS has ITER relevant geometry, it's main goals are provide variant supports for ITER research. Train students as possible ITER staff is one of them.

COMPASS had been designed in eighties in Culham Science Centre. Since 1989 to 2002 COMPASS had been operational in Culham. Spherical tokamak called MAST was installed in Culham in 2002. COMPASS was moved to The Academy of Sciences of The Czech Republic due to lack of resources for COMPASS. Since 2008 COMPASS has been operational in Prague.

COMPASS research potential has not been reached yet, research will be continued. Research goal is mainly edge plasma physics (H-mode studies, Plasma-wall interaction). For the time-being (February 2011) COMPASS is operational, however many diagnostics are missing. Diagnostics, which were installed already, are interferometer, magnetic diagnostics, fast camera for visible light, bolometers, langmuir probes in the divertor, vertical reciprocating probe, near ultraviolet and visible light spectrometers etc. One of the incomplete diagnostics is visible tomographic diagnostics, which will be discussed in this paper too.

Chapter 2

Optical diagnostic

2.1 Plasma parameters we are interested in

Electromagnetic waves are produced by plasma, thus their detection and analysis are desirable. Researchers are usually interested in different wavelength ranges. Plasma visible radiation analysis will help us to understand better plasma-wall interaction, to study hydrogen recycling processes, impurity influx mechanisms and to estimate effective ionic charge.

Measured signal corresponds to incident plasma radiation incoming to detector. The *radiant flux* $\Phi[J s^{-1}]$ is defined in SI derived units [13] as $\Phi = dE/dt$, where $E[J]$ is radiant energy and $t[s]$ time. Another important quantity defined in SI derived units is *radiance* $L[W m^{-2} sr^{-1}]$ defined as

$$L = \frac{d\Phi}{dA \cos \Theta d\Omega}$$

where $A[m^2]$ is area, $\Omega[sr]$ solid angle, $\Theta[rad]$ angle between the normal of the surface element dA and the direction of the radiation, see 2.1, [7].

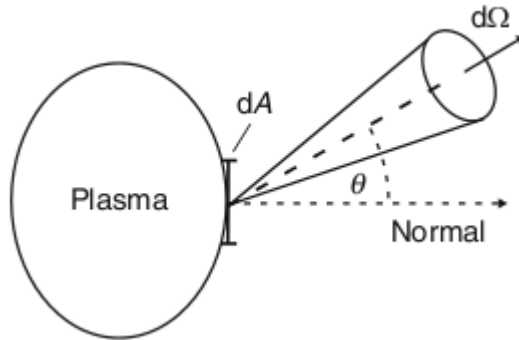


Figure 2.1: Plasma radiance [7]

In our case spectral quantities usually will be used. Spectral quantities are usually marked by λ subscript. For example, radiance $L[W m^{-2} sr^{-1}]$ has corresponding spectral radiance $L_\lambda[W m^{-2} sr^{-1} m^{-1}]$ defined as

$$L = \int L_\lambda(\lambda) d\lambda$$

In general, there are three basic plasma radiations: bound-bound, bound-free and free-free radiations. Bound-bound radiation corresponds to deexcitation of particles and is represented

by narrow peaks in plasma spectrum. Photon energy ν released from particle decay from p level to q level can be calculated according to

$$\nu_{p \rightarrow q} = \frac{E(p) - E(q)}{h}$$

Finally, the lines are not delta functions just because of several broadening mechanisms. In tokamak plasma natural broadening, doppler broadening, Zeeman broadening and stark broadening take place. Doppler broadening is dominant.

Bound-free radiation caused by photorecombination has continuum spectra restricted from one side. Photon with energy

$$h\nu = E_K + E(\infty) - E(q)$$

is emitted during the photorecombination, where E_K is kinetic electron energy, $E(q)$ energy of electron at q level.

Finally, free-free radiation is caused by charged particle deceleration (bremsstrahlung). The radiation has continuum spectra. Bremsstrahlung power P_{Br} can be expressed as

$$P_{Br} = \frac{e^2 a^2}{6\pi\epsilon_0 c^3}$$

where e elemental charge. a is the acceleration caused by Coulomb collisions

$$a = \frac{Ze^2}{4\pi\epsilon_0 m_e r^2}$$

Plasma composition can be gathered by bound-bound radiation analysis. Each line corresponds to a certain ion deexcitation. Thus, if the line is found, the impurity has to be present in plasma.

state	λ [nm]	state	λ [nm]	state	λ [nm]	state	λ [nm]
C V	227.0	C III	464.7	He I	504.8	C III	569.6
O V	278.1	C III	465.0	N V	506.8	C II	588.9
B IV	282.1	C III	465.1	C II	514.5	O V	633.0
O III	304.7	C IV	465.8	Be II	527.0	N V	634.3
O IV	306.4	He II	468.6	N V	527.5	O V	646.6
H I (H δ)	410.2	He I	471.3	C VI	529.0	H I (H α)	656.3
O V	412.4	H I (H β)	486.1	C II	503.2	D α	656.1
N V	433.3	D β	486.0	O V	511.4	C II	658.1
H I (H γ)	434.0	He I	492.2	C II	534.2	He I	667.8
O V	454.9	C V	494.5	He I	541.1	He I	706.5
N V	460.4	HeI	501.6	O V	559.8	He I	728.1
N V	462.0	C II	503.2	N II	567.9		

Table 2.1: Spectral lines planned to be monitored [2]

Plasma rotation can be studied by Doppler shift of spectral lines. The Doppler shift can be found according to relationship based on wavelength measurement

$$\Delta\lambda = \lambda - \lambda_0 = \frac{v\lambda_0}{c}$$

where λ is shifted wavelength, λ_0 is tabulated wavelength, v ion velocity and c is light speed.

Plasma temperature can be estimated from Doppler broadening of spectral line. Spectral line has Gaussian profile due to Doppler broadening. The temperature can be derived from FWHM due to relationship

$$\Delta\lambda_{Doppler} = \sqrt{\frac{8kT_i \ln 2}{mc^2}}$$

where λ wavelength, T_i ion temperature, c light speed, m ion mass, k Boltzmann constant.

Impurity inflow is big tokamak issue. An advantage is possibility to regulate the heat flux onto the wall by proper impurity manipulation. Also noble gases can be beneficial. On the other side, impurity radiation in plasma core is parasitic, which is problem mainly during the ionization, because a lot of impurities get to confined volume. In general, heavy impurities with big atomic number are the most dangerous because of strong energy losses during their ionization.

On average each plasma ion goes to the wall and returns to the plasma many times during the discharge. This process is called recycling. For proper recycling description new coefficient C is defined as ratio of returning particle flux Φ_{ret} to incident flux Φ_{inc}

$$C = \frac{\Phi_{ret}}{\Phi_{inc}}$$

Adsorbed gas can be released to plasma from the wall. An ion particle can be backscattered back to plasma or trapped in wall, where various processes can happen. The impurity can diffuse into solid, form gas molecules, and than it can be released back to plasma after some time.

The neutral atoms can be released to plasma due plasma sputtering. The effects of neutral atom flux from wall can not be neglected. The neutral atoms cause energy losses during their ionization. Collision rate of neutral atoms with plasma particles is $n n_0 \langle \sigma v \rangle$, where n is plasma density, n_0 neutral atom density and $\langle \sigma v \rangle$ reaction rate. For the neutral flux $\Phi_N(r)$ at radius r

$$\Phi_N(r) = \Phi_N(a) \left(1 - \int_r^a \frac{n_e(r) \langle \sigma v \rangle}{\nu_0} dr \right)$$

where $\Phi_N(a)$ initial neutral flux.

One of quantities we are interesting in is effective ionic charge Z_{eff} defined as

$$Z_{eff} = \frac{\sum_{i,z} z_i^2 n_z^i}{\sum_{i,z} z_i n_z^i}$$

where n density and z atomic number of the specie. It can be calculated from bremsstrahlung radiation in line free region. The 523 nm wavelength will be used in our case. The relationship between bremsstrahlung and Z_{eff} is

$$\frac{dN}{d\lambda} = 3.10^{-21} \frac{\bar{g} n_e^2 Z_{eff}}{\lambda \sqrt{T_e}}$$

where \bar{g} is temperature averaged Gaunt factor.

2.2 Diagnostic structure

The visible light diagnostic will consists of few spectrometers and multichannel diagnostic. Czerny-Turner spectrometers had been manufactured by Ocean Optics. It allows to measure

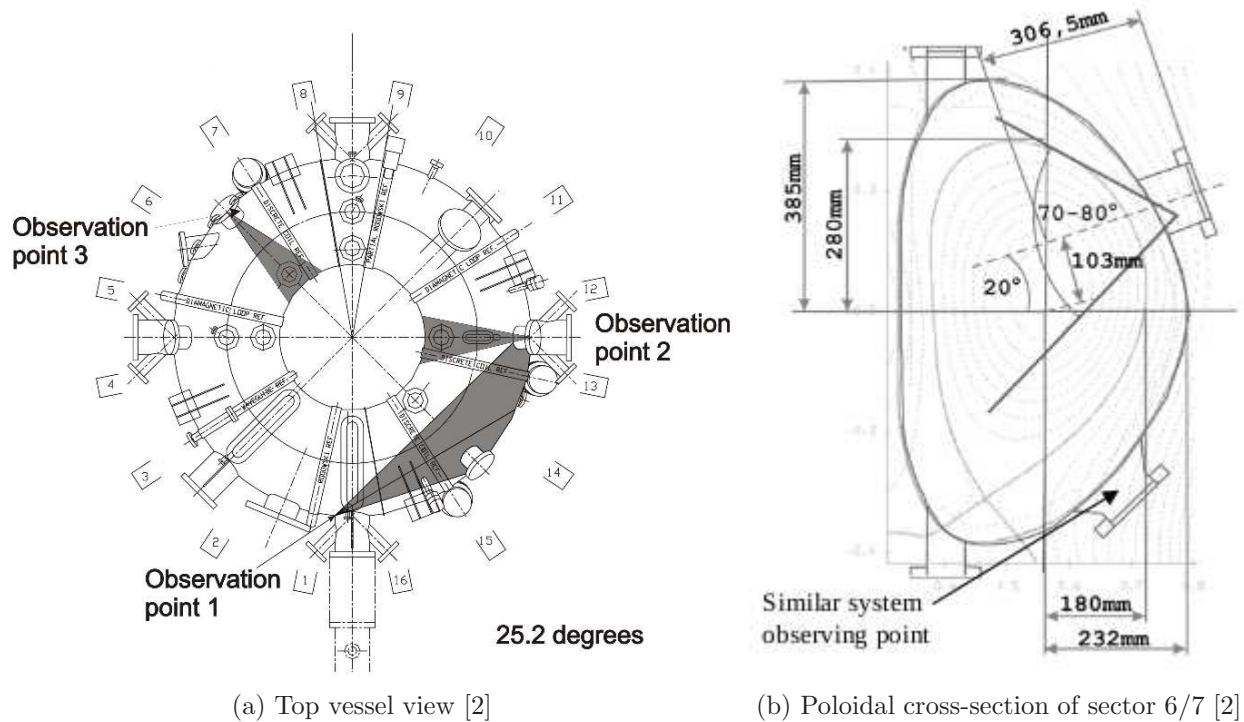


Figure 2.2: COMPASS vessel views

the most intensive spectral lines of impurities. The spectrometer has temporal resolution 1 ms. Multichannel diagnostic with spatial resolution less than 1 cm and temporal resolution up to $1 \mu\text{s}$ will be installed too. The multichannel diagnostic will measure only one selected wavelength or integral VIS. The data will be used for tomography reconstructions of plasma radiation. Code based on reverse Abel transformation will be used.

The spectrometers and the multichannel will be installed in the same port, which will be observation point 3 in section 6/7 at Fig.2.2a. "Sandwich" structure plug has been designed for visible light, soft X-ray and bolometry measurements. Since tomography requires at least two observation points, two the same parts were developed. Upper and lower poloidal ports at the same poloidal cross-section will be used, see Fig.2.2b. Optical system views 110° angle. Both plasma core and plasma edge will be observed.

However, the VIS detectors will not be present in the ports. The detectors are sensitive to tokamak X-ray radiation, thus they will be installed in shielded room. The detectors will be connected with observation point 3 by twenty-meter long optical cable with 37 optical fibres. Transmittance of optical fibres is better than 95%. Two spectrometers will be connected by 2 fibres either to upper port, or to the lower one. Two stage 70-channels amplifier will amplify signal from two multichannel detectors, which register 35 upper light signals and 35 lower light signals.

Except the mentioned VIS diagnostic, few photomultiplier tubes will be installed at some tokamak ports too. The photomultiplier tubes will measure plasma radiation for one wavelength only using interference filter. The photomultiplier's data can be interpreted by FLYCHK code. Another VIS diagnostic are present at tokamak, however they are not goals of the paper.

Chapter 3

The multichannel diagnostic

3.1 Description of the multichannel diagnostic

The tomographic system consists of HXR, bolometry and visible light systems. The plasma volume can be observed in multiple spectral ranges at once. VIS diagnostic will be described. The spatial resolution of the multichannel diagnostic is approximately 10 mm in poloidal direction and the temporal resolution is up to 1 μ s, more parameters are shown in Tab.3.1. The VIS will measure plasma radiation. The diagnostic consists of optical systems build in two poloidal port plugs. Each port plug is connected to one detector array by 35 optical fibres. Signal from each detector goes through the amplifier and ends up in computer.

Both port plugs are the same. Except the visible diagnostic each port plug will carry others diagnostic. Bolometers and soft X-ray diagnostic will be installed in the same port plugs. Bolometers are based on resistivity change due to incoming radiation. X-ray diagnostic measure radiance in X-ray range, which helps understand magnetohydrodynamic instabilities.

The plug consists of several parts. A shutter is present to protect optics during cleaning glow discharge and protect from an impurity deposition during shots when measurement will not be provided. An internal cooling is present to protect HXR and bolometer during vessel baking. However the VIS diagnostic does not need it. The port plug consists of a inset and a flange. The inset holds detectors, air slits, the shutter, cooling channel and optics. The NW100 flange takes in two electrical feed through, rotary feed through in NW16 flange for shutter manipulation, viewport in NW35 flange. However, neither rotary neither electrical feed through are not part of VIS diagnostic.

High vacuum tightness 10^{-6} Pa, heat immunity to 150°C, neutron fluxes resistance, transparency for 400-800 nm range are required. Thus NW35 is Spectroil 2000 UF fused silica

Parameter	Value
Number of detector arrays	2
Number of channels per detector	35
Rise time	0.1 μ s
Maximal sensitivity	0.5 A/W
Spectral response	190 - 1000 nm
Signal range	0 - 4.7 V

Table 3.1: Multichannel diagnostic parameters

vacuum window, which was made by Vacom. The inset has been made monolithic, see Fig.3.1. The design makes the inset difficult to manufacture. Thus, the inset has double flange structure. The first flange contains cooling channel with 6 mm diameter, the second one links the NW100 flange to the inner inset. Moreover, the design allows port plug assembly before connecting to port.

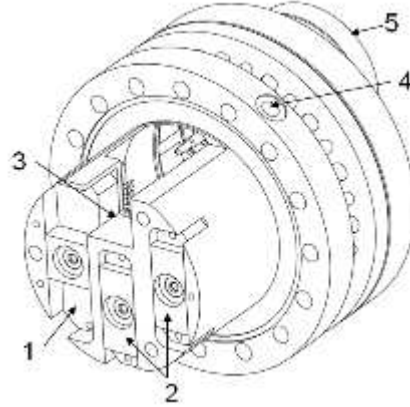


Figure 3.1: Multichannel diagnostic port detail. 1 Soft X-ray detector, 2 Bolometers, 3 Focusing system space, 4 Hole for cooling, 5 Vacuum window flange. [2]

The optical system in port plug consists of objective, in-line window NW35, interference filter and linear optical fibre set. The objective collimate incoming light into a parallel beam on the fibres side. The observation angle is up to 110° . The parallel beam goes into by optical fibres directly.

Main reason for UF fused silica is high transmittance. Fused silica with high OH will be used, it's transmittance is showed in Fig.3.4. Fortunately, the transmittance is over 95% in our range of interest. Used optical fibres have $200\ \mu\text{m}$ core radius, another $40\ \mu\text{m}$ cladding layer and $160\ \mu\text{m}$ buffer layer. The numerical aperture of used fibres is $\text{NA} = 0.22$. Each of two parts of the visible diagnostic optical cable consists of 37 fibres. Since two fibres will be used by the spectrometer HR2000+ discussed before, the rest of 35 fibres will be used by the multichannel. SubMiniature version A (SMA) connectors will be used for better flexibility at the detector end.

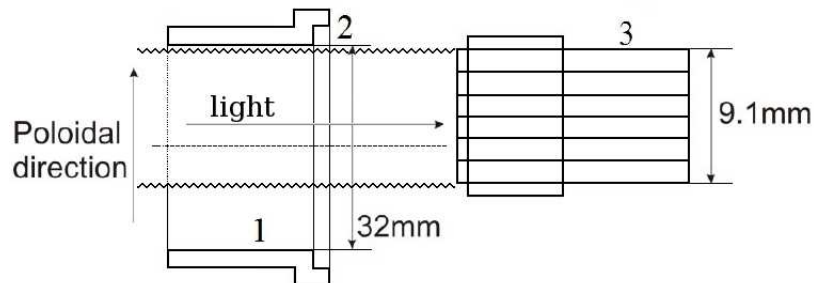


Figure 3.2: Tokamak side view of fibres connection: 1 air side of diagnostic port enclosure, 2 vacuum window, 3 row of fibres [2]

Each of two detector photodiode arrays S4114-35Q manufactured by HAMAMATSU is able to detect 35 light signals, see Fig.3.5a. Some photodiode properties are shown in Tab.3.1.

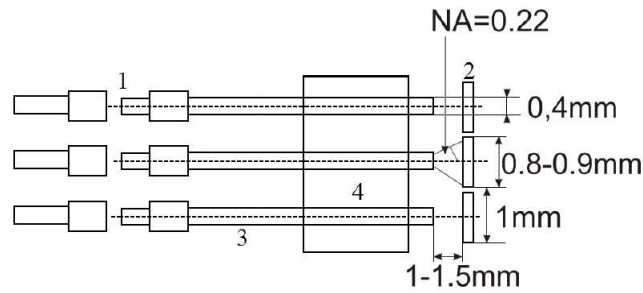


Figure 3.3: Detector side view of fibres connection: 1 SMA connector, 2 detectors elements, 3 fibres, 4 fibres holder [2]

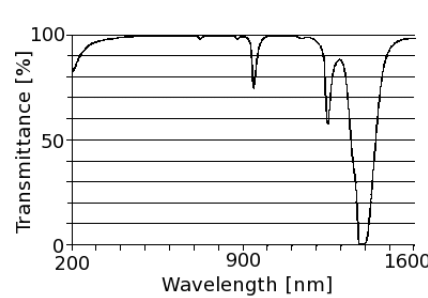


Figure 3.4: Optical fibre transmittance

Strong wavelength photosensitivity dependence is big disadvantage. On the other side, low photodiode price is great advantage.

Since detectors produce low current, an amplification are needed. The detector current signal is converted to voltage signal at first. Than the voltage signal is amplified approximately 500 000 times. The general schema of the two stage 70 channel amplifier showed at Fig.3.6 are following. Signal registration range is 0-5 V. Amplification noise level is 2 mV. Temporal resolution has limit 1 MHz. However, few important limitations discussed below have to be concerned.

The detector current is linear dependent at power of incoming light. Its range is 0.01 - 1 μ A. Since this low current has to be converted to voltage, current conduct is highly limited in background with strong electromagnetic field. Thus, preamplifier or amplifier has to be placed near the detector. Also the whole electrical network has to be shielded properly.

Another limitation is output cable length limitation. The amplifier output connection with computer card has to have the lowest impedance possible. Thus, the resistor R4 is present on the scheme at Fig.3.6. Its value for maximal voltage +5 V should be in range 680-1000 Ω . Also the maximal allowed current output 10 - 20 mA should be used. Power supply voltage is +5 V. However the current overload and power supply voltage overload have to be prevented.

Furthermore, sampling frequency of data collection is 2 MHz. According to theory, transmitted frequency has not to reach one half of the sampling frequency, thus it should not reach 1 MHz. However, frequency range of used detector can overload the maximal frequency.

Artificial ground has been set to +4.7 V, because detector output is negative signal. The low detector signal should be conducted with the artificial ground. Otherwise parasitic current appears.

Since the output cable capacity can be usually in range of 100 pF - 1 nF, a resistor should be plugged in set with the amplifier output. Another solution is use resistor R4 at schema. In

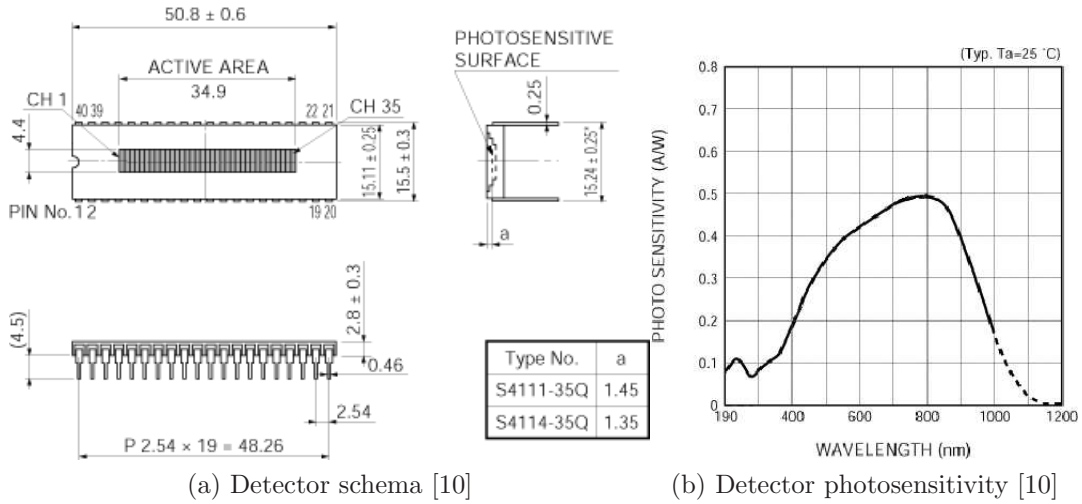


Figure 3.5: S4114-35Q HAMAMATSU Detector [10]

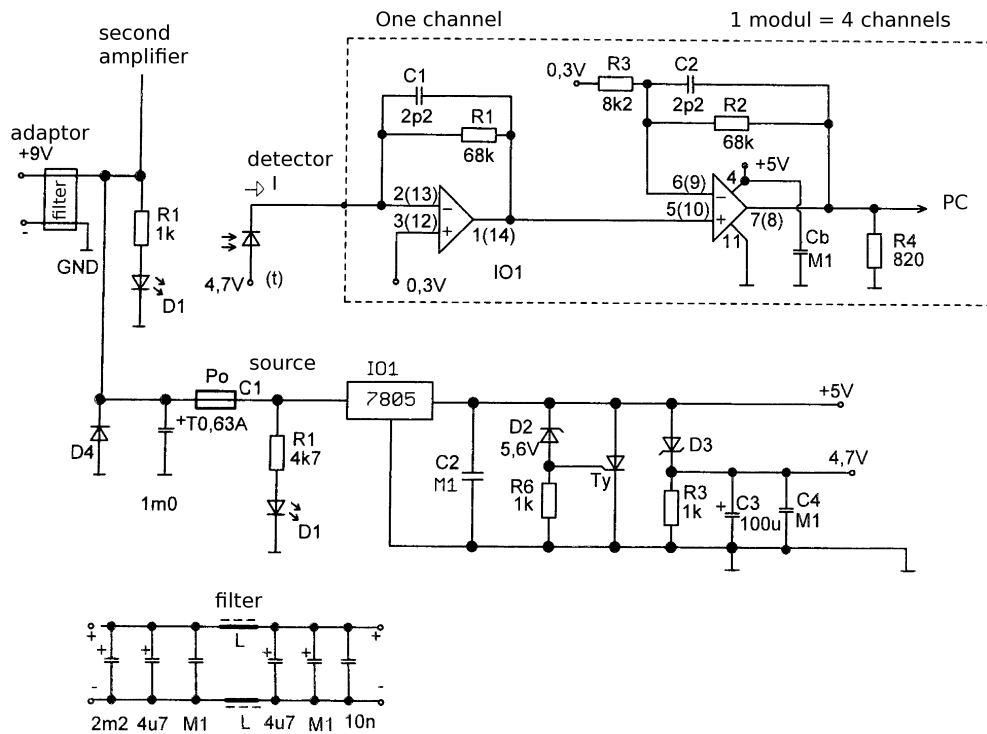


Figure 3.6: Amplifier schema [9], one channel schema using one half of the guard operational amplifier

Part	Value	Type	Part	Value	Type
R1, R2	47k Ω	SMD1206	C6	100pF	ceramic
R3	4.7k Ω	SMD1206	Cb	100nF	SMD1206
R4	1k Ω	SMD1206	D1		BZX83V013
R6	1k Ω	miniature	D2		BZX83V005.6
R7	1k Ω	miniature	D3, D4, D5		BAT46
R8	100k Ω	miniature	D6		LED
R9	220k Ω	miniature	D7		1N4007
R10, R11	1k Ω	miniature	IO1		MCP6024
C1, C2	3.3pF	SMD805	IO2		555C
C3	1mF/16V	radial	IO3		MA7805
C4, C7, C10, C11	100nF	ceramic	Ty		MCR100-8
C5, C8, C9	100 μ F/16V				

Table 3.2: List of amplifier's components

other case, circuit instability is on the way.

Due to strong electromagnetic field, the amplifier's power supply has overvoltage protection. The amplifier design allows good access to all parts and also it's maintainance. As base card connectors have been used BL250G connectors, as module connectors have been used S2G50W and BLW250G connectors. The distribution frame has been used ARK300V-2P. Since there are 2 x 35 fibres, computer records 70 signals. Computer save the signal to ATCA database. Researchers access the data by GARP program.

3.2 Amplifier's "time constant" measurements

The VIS amplifier, see Fig.3.6, converts the given current signal to voltage signal. The output voltage signal is approximately 500 000 times stronger than the input signal. For proper amplifier usage a time constant calibration is needed. A lag happens when sharp signal arises during the amplification. This lag is described by a time constant.

Time constant comes from linear time-invariant (LTI) system theory. The time constant is able to describe the first-order LTI system, in our case the amplification process. In general, the LTI first-order system is described by equation

$$\frac{dV}{dt} + \frac{V}{\tau} = f(t)$$

with solution

$$V = V_0 e^{-t/\tau}$$

where τ is time constant representing the downfall or decay, t is time, $f(t)$ external function, V_0 is initial value.

The experimental setup is shown at Fig.3.7. Common photodiode accept signal from trigger and produces short light signal. The amplifier manages the current signal from detector. Finally, the data collection system saves the signal. Noise was approximately 2 mV.

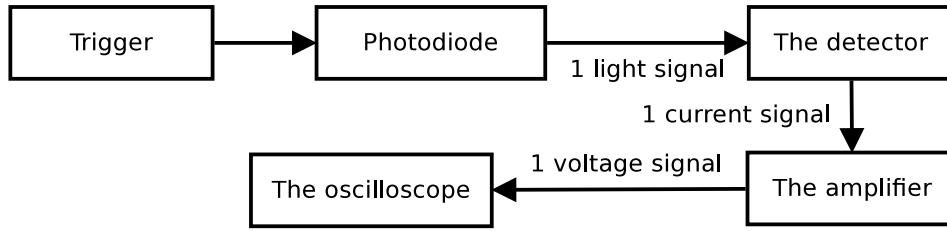


Figure 3.7: Experimental setup of time constant amplifier calibration

Signals for all 70 channels were received, example for one of channels at Fig.3.8a. Time constant can be calculated by the curvefit function. The IDL's curvefit function uses a gradient-expansion algorithm and it serves for a non-linear least squares computation [16]. The time constant $\tau = 4.92\text{e-}07$ s was calculated. The compare of measured signal and time constant approximation is showed at Fig.3.8. Time constant for some of channels are shown at Tab.3.3 as the final time constant.

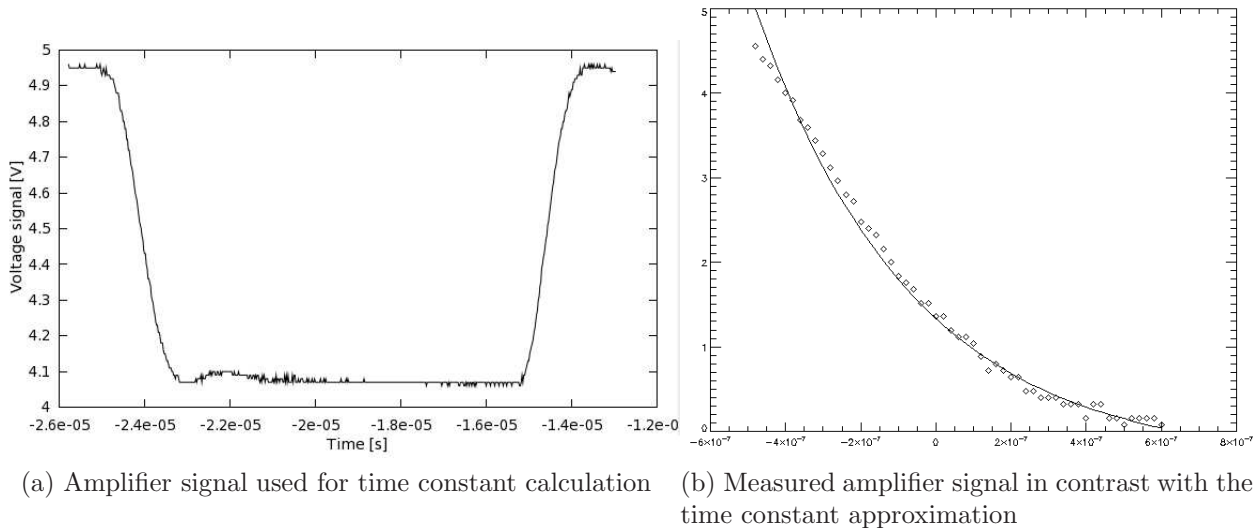


Figure 3.8: Time constant calibration results

3.3 Detector sensitivity tests

The CCD detector S4114-35Q consists of 35 detector circuits as shown at Fig.3.5a. Each circuit is independent and can convert the same light signal to different voltage. Thus, a non-uniformity is possible. The non-uniformity has impact on total diagnostic accuracy.

A lamp produces homogeneous light. Thus, an incident light from should be same for all 35 detector circuits. Total radiance is measured by each detector circuit and 35 currents are produced. Each current signal is managed by the amplifier and 35 voltage signals are send to data collection system. Experimental setup is shown in Fig.3.9.

The 1th channel was used as reference channel, the results are shown in Fig.3.10. Deviation from average value is less than 5%. Small non-uniformity was expected due to detector (elements uniformity), lamp (external effects) and experimental setting (light comes through air). The results agree with the expectation, a small non-uniformity was measured.

Measurement	Time constant
0	4.83753e-07
1	4.63398e-07
2	4.36165e-07
3	4.22400e-07
4	3.97939e-07
5	5.10087e-07
6	4.46086e-07
7	4.63681e-07
8	5.19588e-07
9	5.51502e-07
10	6.78223e-07
11	5.34178e-07
$\tau[s]$	4.9225e-07

Table 3.3: Time constant calculation using IDL’s curvefit function

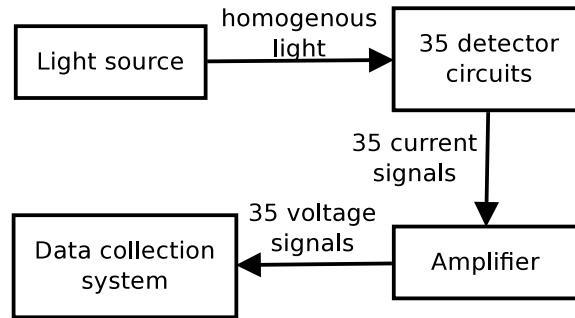


Figure 3.9: Schema of detector intensity calibration experiment

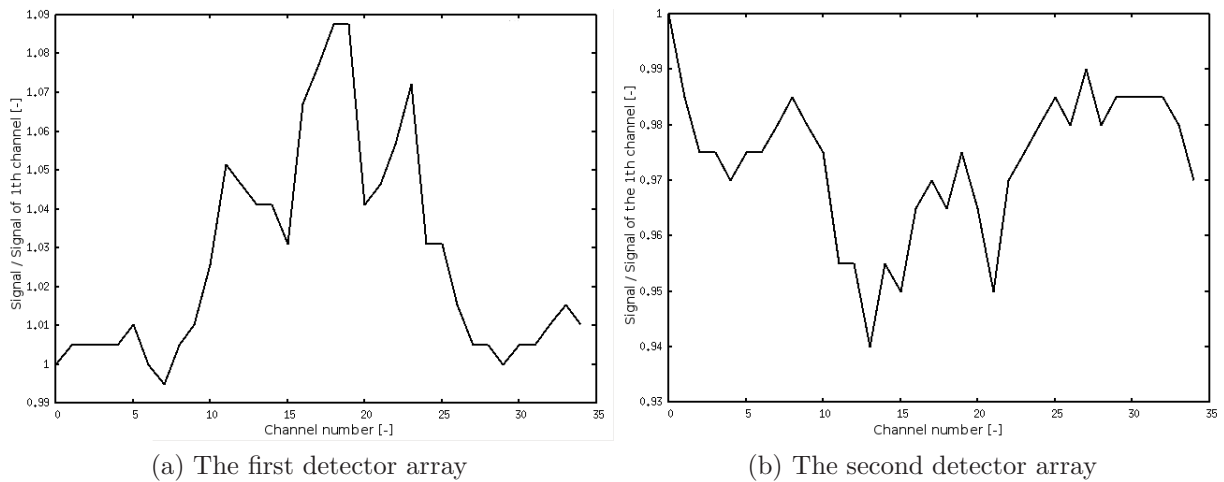


Figure 3.10: Results of detector sensitivity calibration, ratio of light intensities of i -th and 1th channel dependent on channel’s number for homogeneous light source

3.4 Alignment

The optical fibres are spaced to detector protection glass directly, gap is always present. The light divergence causes overlaps, see Fig.3.11. The distance between the detector surface and the fibres should be minimal. If the gap is too big, mechanical changes are required. The question is how much this phenomenon inflicts the results. If the stray light is too high, the results can be useless and the connection between fibres and detector has to be rebuilt. Accuracy of the multichannel diagnostic depends at the overlapping strongly. At the beginning of the measurement the gap was approximately 1.35 mm, overlapping was less than 20%. After it was changed to 0.35 mm.

At the first side, header contains linear set of 35 optical fibres. Each fibre core diameter is 0.2 mm. The distance is 1 mm between axis of two neighbour fibres in the header. On the other side, CCD array contains 35 detector elements. Each one is 0.9 mm wide. The distance between two elements in the detector array is 0.1 mm, see Fig.3.3. The detector surface is protected by glass.

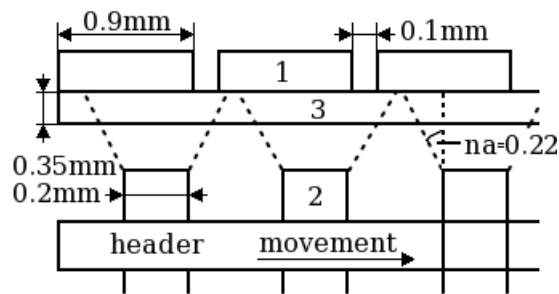


Figure 3.11: Connection between the optical fibre and the detector array: 1 - detector element, 2 - optical fibre, 3 - detector surface

Experimental setup is shown on Fig.3.12. Homogeneous white light source HL-2000 is connected to the detector through one optical fibre. Since header contains 35 fibres and only one is used, 34 fibres should be dark. Main signal from appropriate detection circuit is recorded. Noise from side circuits are recorded too. Detector signals are amplified by the amplifier and processed by an oscilloscope DS1102E.

The goal of the first experiment was find the best header position. Thus, the header position is changing during the first measurement, see Fig.3.11. Voltages of four neighbour channels (2nd - 5th) were measured as a function of detector position in range -5 - +5 mm, see Fig.3.13. There are four different signals shown together from four different detector channels. The best header position was set as result.

During the second measurement the best header position is already set. Now, each of 35 detector channels has to be measured with its left and right neighbour detector channels. Thus, during the measurement the light source is step by step connected to each channel and the appropriate channel and neighbour channels are measured.

Signal overlapping is less than 6 %. Since the header will be take off after the measurement, another calibration will be needed again in the final state. However, final position value should be similar.

The overlapping signal is shown for all 35 channels, both detectors, see Fig.3.4 and Fig.3.15. The border channels have only one neighbour channel, thus a values are missing. The fourth signal has been chosen as reference channel for the first detector, the 1th channel for the second

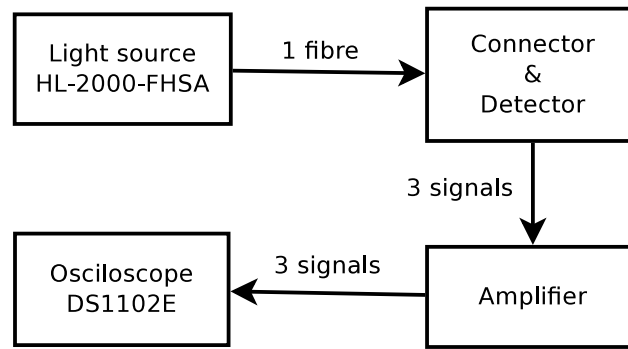


Figure 3.12: Experimental setup of alignment calibration

detector. The reference channel of the Fig.3.4 is the lowest one. On the other side, the reference channel of the Fig.3.15 is an average one. Also each detector was connected to similar, but little different fibres holder. Each connection parameters were also a little different. Thus the ratio of main and neighbour signals differ for each detector. However, the overlapping signal ratio is quite low, up to 6%. Thus, a calibration constant has to be set for each channel, which will characterize this overlapping.

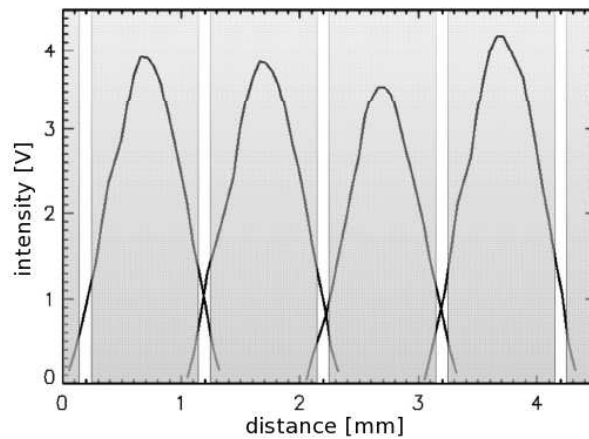


Figure 3.13: Four different signals from four neighbour channels in dependence on header position [2]

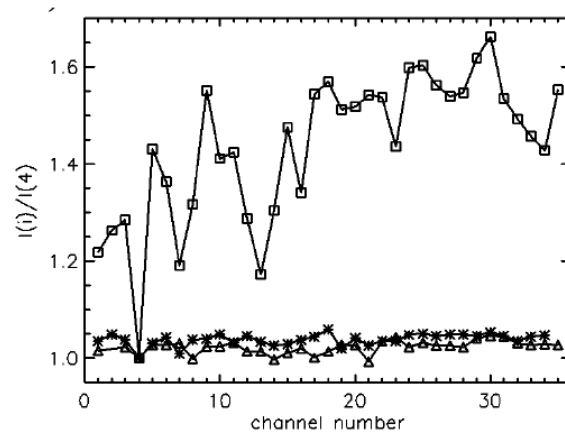


Figure 3.14: Main detector signal and overlapping signals from left and right neighbour detector channels for the best header position [2] for 1th detector array

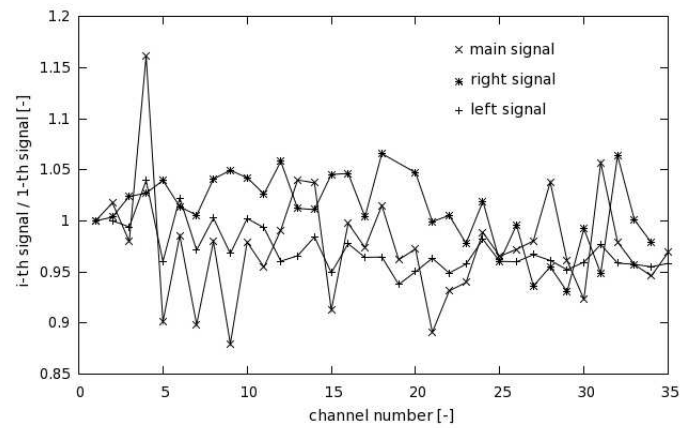


Figure 3.15: Main detector signal and overlapping signals from left and right neighbour detector channels for the best header position for 2nd detector array

Chapter 4

Spectrometers

4.1 Description of the spectrometers

Two HR2000+ High-speed Spectrometers had been purchased from Ocean Optics. The range of the first one is 247-472 nm, range of the second one is 457-663 nm. The aim of the spectrometers is measure impurity spectral lines.

Czerny-Turner spectrometer design is shown at Fig.4.1. The most common design consists of two plane mirrors and one plane grating. The light goes through entrance slit and is focused to the grating by focusing mirror. Diffracted light from the grating is collimated to detector. This design excludes coma effect and keeps astigmatism low. Also no light deformation happens since the absence of lens and prisms. However, industrial accuracy is required and proper mirror positioning needed. Otherwise diffracted light can hit collimating mirror again. Since visible light is measured, air in spectrometer is allowed.

The internal process of the HR2000+ High-speed Spectrometer is show at Fig.4.1. The slit regulates amount and resolution of light coming inside. Interference filter can be added after the slit. Sony ILX-511 linear silicon CCD detector convert incidence light to a voltage signal. The CCD array consists of 2048 pixels with sensitivity 75 photons per count at 400 nm or 41 photons per count at 600 nm. Size of pixel itself is 14 μm times 200 μm and well depth is 62.500 electrons. Signal to noise ratio is 250:1 at full signal. Important spectrometer parameter is stray light, which had been set less than 0.05 percent at 600 nm or less than 0.10 percent at 435 nm. Signal integration time lies in range of 1 ms - 65 s. Others parameters can be found at device manual [8].

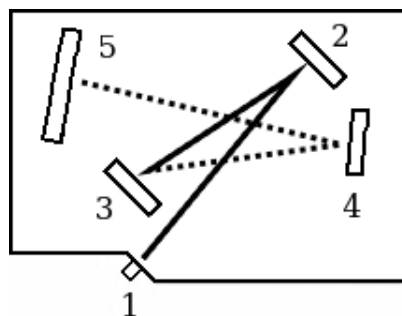


Figure 4.1: HR2000+ spectrometer Czerny-Turner structure: 1 - SMA Connector with slit and filter if needed, 2 - focusing mirror, 3 - the grating, 4 - collimating mirror, 5 - CCD detector [8]

As mentioned before, both spectrometers will be connected by the optical cable either to upper port at section 6/7, or to lower poloidal port, see Fig.2.2b. The spectrometers have been already connected to observation point 1 and 2 for other measurements, see Fig.2.2a. Time integrated spectra during the discharge was received for example, see Fig.4.2.

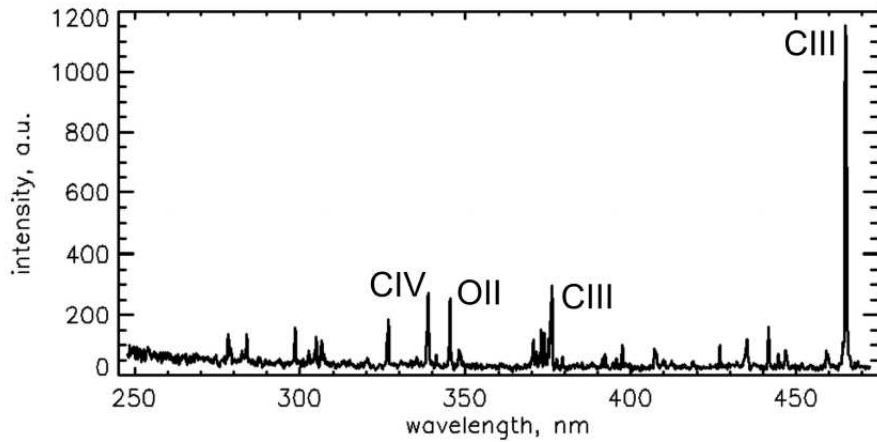


Figure 4.2: Example of measured spectra by the spectrometer at port position 2 [3]

4.2 Spectrometer calibration

Spectrometer consists of several hi-tech parts as discussed before. The grating, detector and lens are very sensitive to manipulation with them. Improper manipulation influences internal settings. Check of calibration have to be proved periodically.

The calibration was done according to [8]. The calibration lamp spectrum measured by the spectrometer should be the same as the tabulated one. The difference between measured and tabulated spectrum should not depend on integration time, neither at others built-in parameters. It should depend only at internal spectrometer math, which can be configured.

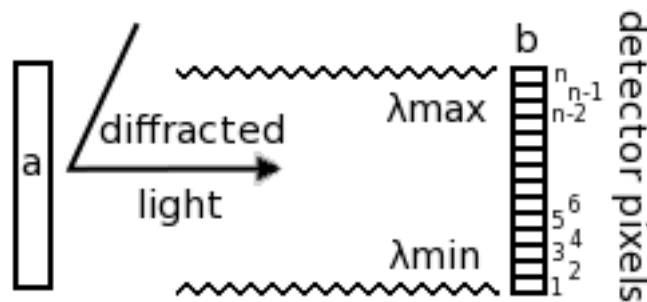


Figure 4.3: Principle of the spectrometer math: relationship between wavelength (of diffracted light from grating) and pixels (which detects the wavelengths). a - collimation mirror, b - CCD detector

The spectrometer's math is based at algebraic equation Eq.4.1.

$$\lambda_p = I + C_1 p + C_2 p^2 + C_3 p^3 \quad (4.1)$$

where λ_p wavelength of the spectral line corresponding to the pixel number, where p detector pixel number, where I, C_1, C_2, C_3 unknown coefficients. The equation represents relationship between hardware pixel position p and corresponding wavelength number λ_p [nm], see Fig.4.3. Since the manufacturer do the calibration at his factory, the variables I, C_1, C_2, C_3 are usually set, however recalibration is needed due to device sensitivity to manipulation (transportation, etc).

The re-set mentioned before consists of solving few algebraic equations for four unknown parameters. In this case at least four wavelength should be measurable in range of interest. The tabulated wavelength are provided by manual of used light source. Spectrometer measurement provides a pixel preview of light source spectrum. A difference between measured and tabulated lines may occurs. New parameters have to be calculated. The tabulated wavelength peaks have to agree with measured pixel peaks. The parameters are found by solving the set of few equations.

When new coefficients are found and updated into the spectrometer, the calibration is done. The update is made by spectrometer software provided by the manufacturer via USB.

The experiment is done for both spectrometers. The experimental setup is illustrated at Fig.4.4. CAL-2000 light source is connected to the spectrometer by optical fibre. The spectrometer signal is processed by Ocean Optics Spectral Suit software. The integration time was set to 20 s in first calibration, 6 s in second one, however the results do not depend at integration time. We used 5 μm wide slit and we used appropriate filter. Also we skip L2 detector collection lens.

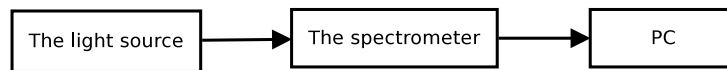


Figure 4.4: Schema of spectrometer calibration

Data in Tab.4.1 are gained according to discussed procedure. Next the Matlab third-linear regress function is used to calculate the unknown coefficients I, C_1, C_2, C_3 . However, the first measurement at spectrometer with range 457-663 nm failed, because three spectral lines are not enough for calibration. At least the second measurement at range 247-472 nm was successful with nine spectral lines. Extracted coefficients are shown in Eq.4.2 given by regress function. The R-square value is one minus the ratio of the error sum of squares to the total sum of squares [11]. Thus, check parameter R^2 should be close to one for valid output data. If it is not, some kind of mistake happened. New coefficients are updated to the spectrometer only for the second spectrometer. The measurement for the first one should be repeated with different light source with more spectral lines in it's range. The second one was successful, which the R-squared statistics indicate.

$$\lambda = 2.4753^{-7} + 1.1964^{-10} p - 6.0136^{-15} p^2 + 6.6439^{-19} p^3 \quad (4.2)$$

where $\lambda[m]$ wavelength of the spectral line corresponding to the pixel number, where p detector pixel number.

Tabulated λ [nm]	Measured pixels p[-]	Calculated λ [nm]	Error [nm]
253.652	51	253.6157	0.0363
296.728	422	296.9965	-0.2685
302.150	470	302.5008	0.3508
313.155	556	312.3044	0.8506
334.148	752	334.3803	-0.2323
365.015	1030	365.1044	-0.0894
404.656	1396	404.6343	0.0217
407.783	1425	407.7269	0.0561
435.833	1691	435.8566	-0.0236

Table 4.1: UV spectrometer (247-472 nm) calibration, the tabulated spectral lines by light source manufacturer [12], measured pixel values by the spectrometer and calculated wavelengths of the spectral lines according to new equation Eq.4.2

Chapter 5

Photomultiplier

5.1 Photomultiplier tube description

The photomultiplier tubes (PMT) measures total radiance of incoming light and produces voltage signal. Advantage of the PMTs is linearity, high sensitivity, low noise, possibility of using interference filter, etc. On the other side, PMT usage is limited by used materials, which convert photons to electrons, anode material, which absorbs electrons, vacuum quality, the electric voltage divider circuit, ohmic heating, etc.

Schema of PMT is shown at Fig.5.1. Incident radiation cause electron emission from cathode C. The cathode emits amount of electrons corresponding to absorbed energy. The electrons accelerate in electric field, which is caused by potential difference between cathode C and cathode D. The electrons reach D cathode surface and new electrons are released from D cathode. Amount of released electrons from cathode D is bigger than amount of emitted electrons from C cathode. The released electrons are in electric field, which is caused by different potentials between D cathode and next cathode. Each time electrons are accelerated, collide with next cathode and bigger amount of electrons is released. Finally, the electrons comes to anode A, where create measurable signal. The PMT electric circuit is shown at Fig.5.2. It contains voltage divider, which creates cathode potentials.

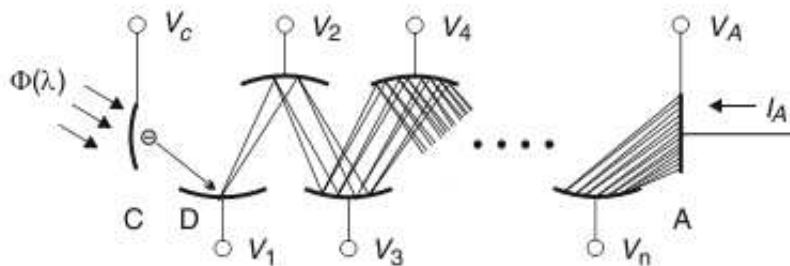


Figure 5.1: Photomultiplier principle [7], C as cathode that releases the electrons, A as anode that accept the electron flux and create the signal, V as dynodes that speed up the electrons and amplify the electron flux

Proper knowledge and regulation of voltage divider is needed in order to secure stable power supply. The ratio of anode current I_A and resistor current I_R should fulfil

$$\frac{I_A}{I_R} \leq 0.01$$

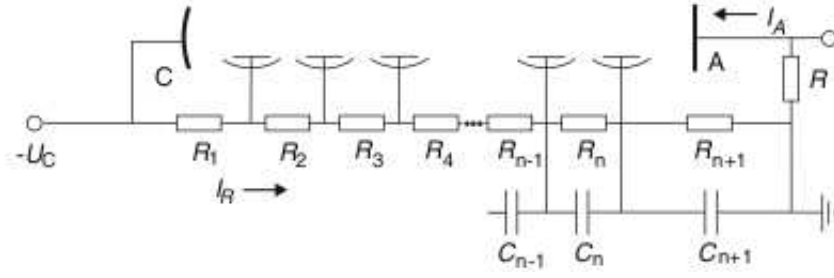


Figure 5.2: Photomultiplier's voltage divider [7]

otherwise an amplification anomalies can happen. Another important topic is ohmic heating, which influences the amplification process and photomultiplier's lifetime. Thus, a voltage divider current should be usually under $10 \mu\text{A}$ for the most PMTs. Also the time delay is present, usually the electron avalanche takes 20-100 ns. Usually the photomultiplier is used in pulse mode, which allows define new quantities. The rise time usually express time between 10% and 90% of current full level. The frequency bandwidth usually express difference between lower and upper frequencies, at which the amplitude of the current corresponds with $1/\sqrt{2}$ of the peak current level. The rise time T_r is usually 1 - 15 ns and it has relationship with the frequency bandwidth f_{bw}

$$f_{bw} T_r \cong 0.35$$

for common PMT. Another important fact is signal broadening presence. It is created by different electron trajectories, which spreads the signal into wide time range. Also dark current contribute to signal, because thermal emission from cathode and all dynodes exists. A special quantity is defined for PMT called secondary emission coefficient δ , which is average ratio of released electrons and incident electrons. This coefficient depends for example at dynode material, but also at dynode surface or the angle of incidence. Primary electron kinetic energy influences this coefficient too. This coefficient usually do not cross 4 - 14 range at 200 eV electrons. Total gain G quantity is defined as $G = \delta^n$ for n dynodes.

Next big problem is noise, which influences the measurement and it's accuracy. Shot noise $\sqrt{\Delta \bar{I}_D^2}$, Johnson noise $\Delta \bar{I}_R^2$ and photocurrent I_C are present. Photomultiplier bandwidth f_{bw}^* is defined as

$$f_{dw}^* = \frac{1}{2\pi R C_A}$$

where C_A is anode capacitance. The first noise current is connected to the current and the bandwidth according to equation

$$\Delta \bar{I}_D^2 = 2eI\Delta f$$

where $\Delta f \leq f_{bw}$ as bandwidth range of the measurement and e as elementary charge. The second one is connected to the circuit resistor and temperature by Nyquist equation

$$\Delta \bar{I}_R^2 = \frac{4k_B T \Delta f}{R}$$

The third one is defined as $I_C = S(\lambda)\Phi(\lambda)$ with $S(\lambda)$ as spectral photosensitivity and $\Phi(\lambda)$ detected radiant flux. Thus, since all noise currents are independent at each other and since the Johnson noise is negligible, the total anode noise current $\Delta \bar{I}_A^2$ can be calculated as

$$\Delta \bar{I}_A^2 = 2eG^2(I_C + I_D) \frac{\delta}{\delta - 1} \Delta f$$

where the coefficient $\frac{\delta}{\delta-1}$ is present due to fluctuations, see [7]. Finally signal-to-noise ratio can be calculated as

$$\frac{I_A}{\sqrt{\Delta I_A^2}}$$

An important property of PMT is photocathode excitation. This effect happens when the photomultiplier is exposed to non-operational conditions like daylight. The dark current is amplified many times and the dark current relaxation takes several hours.

Scintillator combination with PMT is common usage. This useful trick makes PMT applicable for UV and XUV spectral regions, since the scintillator absorbs radiation and produces radiation in different wavelength range. However, scintillator usage highly damages the total property of the diagnostic.

Photomultiplier tubes will not be installed at the same sector 6/7 as spectrometers and multichannel diagnostic. Many other ports can be used, for example observation points 1 or 2 at Fig.2.2a. It will provide total radiance or spectral radiance if a interference filter will be used. The PMTs measurement can improve understanding of boronization for example.

5.2 Photomultiplier tubes tests

Before PMT usage the amplification has to be described properly. Two photomultiplier tubes with serial numbers VIS3: M10FS25 and VIS1: EMI were tested. The amplification is described by anode signal as function of power supply. The incident radiation should be constant during the measurement.

Setting of the experiment is shown at Fig.5.3. The Halogen Light Source HL-2000 was used during the measurement. The photomultiplier tube has high voltage power supply with variable output 0-2 kV. Trigger pulse had been set to 5 V high and 210 ms long.

Light source was powered and stable during the whole experiment. The PMT's power supply was set on different voltage each time. Output PMT's signal was processed by computer on trigger order. Thus, output voltage signal dependence on power supply voltage was measured.

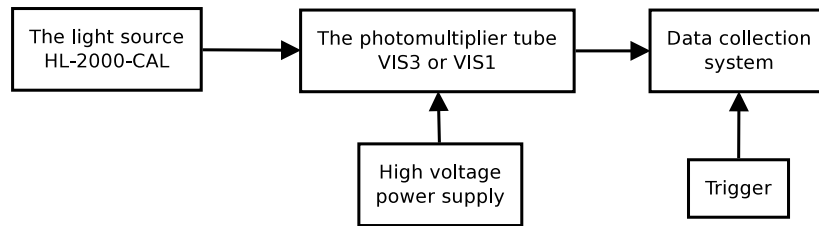


Figure 5.3: Photomultiplier's experiment schema

Measured anode signal dependence on power supply was computed and plotted by IDL Fig.5.4 for both PMTs. The PMT amplification is established by the curves.

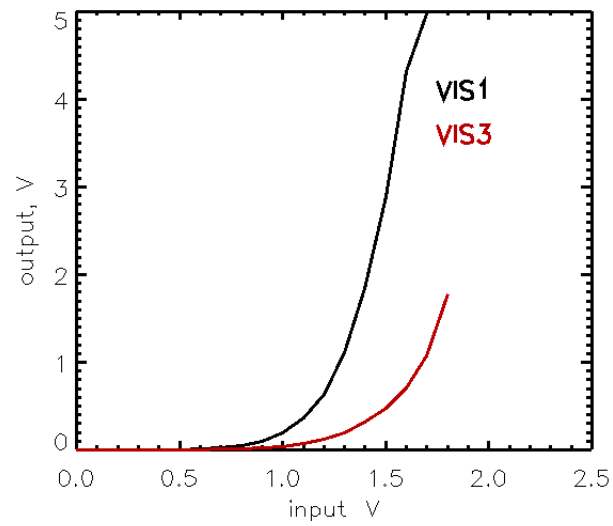


Figure 5.4: PMT's output with respect to PMT's power supply level

Chapter 6

FLYCHK simulation

By means of collisional-radiative model can be described behaviour of working gas in tokamak discharges. This model is used by FLYCHK code developed by National Institute of Standards and Technology. However, the FLYCHK code is quite sophisticated and understanding is quite difficult. Thus, the modelling was done as training only.

6.1 Simulation theory

Collisional-radiative model (CR) is a non-equilibrium model and it is based on idea that population distribution depends on: plasma parameters in the point, local collisional processes, non-local radiative processes. Atomic level populations are essential for analysing measured quantities by CR model. The atomic level populations are determined by collisional and radiative processes.

Rate equations for level populations are constructed with rate coefficients of collisional and radiative processes computed by atomic physics codes. The radiation field needed for computing radiative rate coefficients can be obtained from the radiation transport equation. Since the radiation transport equation involves the population distribution, the CR rate equations and the radiation transport should be solved self-consistently. [18]

The rate equations have following form

$$\frac{dn_i}{dt} = -n_i \sum_{j \neq i}^{N_L} W_{ij} + \sum_{j \neq i}^{N_L} n_j W_{ji} \quad i \in \hat{N}_L$$

$$W_{ij} = B_{ij} \overline{J_{ij}} + n_e C_{ij} + \beta_{ij} + n_e \gamma_{ij} + \sigma_{ij} + I_{ij} \quad i < j$$

$$W_{ij} = A_{ji} + B_{ji} \overline{J_{ji}} + n_e D_{ji} + n_e \alpha_{ji} + n_e \kappa_{ji} + n_e^2 \delta_{ji} \quad j < i$$

where coefficients are listed in the Tab.6.1. The radiation transport equations have following form

$$\left(\frac{1}{c} \frac{\partial}{\partial t} + n \cdot \nabla \right) I(r, n, \nu, t) = \eta(r, n, \nu, t) - \chi(r, n, \nu, t) I(r, n, \nu, t)$$

where $I(\vec{r}, \vec{n}, \nu, t)$ radiation intensity at position \vec{r} in direction \vec{n} with frequency ν , $\eta(r, n, \nu, t)$ emission coefficient and $\chi(r, n, \nu, t)$ absorption coefficient. The numerical solution is based on iteration and solving both equations repeatedly.

Coefficient	Description
A_{ij}	spontaneous emission
B_{ij}	stimulated absorption for $i < j$ or emission for $i > j$
C_{ij}	collisional excitation
D_{ij}	collisional deexcitation
I_{ij}	beam and non-thermal e^- collisions
α_{ji}	radiative recombination
β_{ij}	photoionization plus stimulated recombination
γ_{ij}	collisional recombination
κ_{ji}	electron capture
σ_{ij}	autoionization
n_e	electron density
\bar{J}	frequency-averaged mean transition-relevant intensity
$j\bar{i}$	transition from level j to level i
N_L	number of the levels included in the calculation

Table 6.1: Rate equation coefficient explanation [18]

6.2 Simulation execution

Plasma shot No.1519 has been chosen from COMPASS tokamak shot database. Electron density n_e and hydrogen ionization line H_α were measured at COMPASS tokamak during the shot, see Fig.6.1a and Fig.6.1b. T_e was not measured.

Following parameters were set for the simulation. The impurities were neglected during the simulation, the working gas was only considered as hydrogen with its nuclear charge $Z = 1$. The non-local thermodynamic equilibrium model was set. The density type was set as electron. The ion-electron temperature ratio was not set. FLYCHK process only ten steps at once, thus two separated simulations have been done. The first one started with none ionized hydrogen, the second one started with all ionized hydrogen. Evolution of electron density and electron temperature was provided as an input file, see Fig.6.1a, Fig.6.2a.

The simulation requires electron temperature, however it was unknown from tokamak measurement. On the other side H_α measurement were at disposal. Thus, the electron temperature values were guessed. The calculated H_α results in Fig.6.2b were confronted with theoretical model of plasma discharge in tokamak. If theory did not agree with the simulation result, an iteration was made and electron temperatures were changed by guess again. The simulation was processed again. Finally the result as the estimation of electron temperature evolution in Fig.6.2a was received.

The simulation corresponds with theory for given electron density Fig.6.1a and temperature Fig.6.2a. The measured H_α signal in time range 962-969 ms is caused by plasma wall interaction and it is not possible to model. Also signal since 971 ms is not possible to model. On the other side, the strong first peak at 961.5 ms and small second peak at 970 ms can be modelled and corresponds with plasma ionization and plasma recombination. The steady level of 30 eV can be changed with no impact on H_α shape due to full plasma ionization. During this stage it could be 25 eV or 35 eV as well. Different H_α peak strengths correspond with difference between

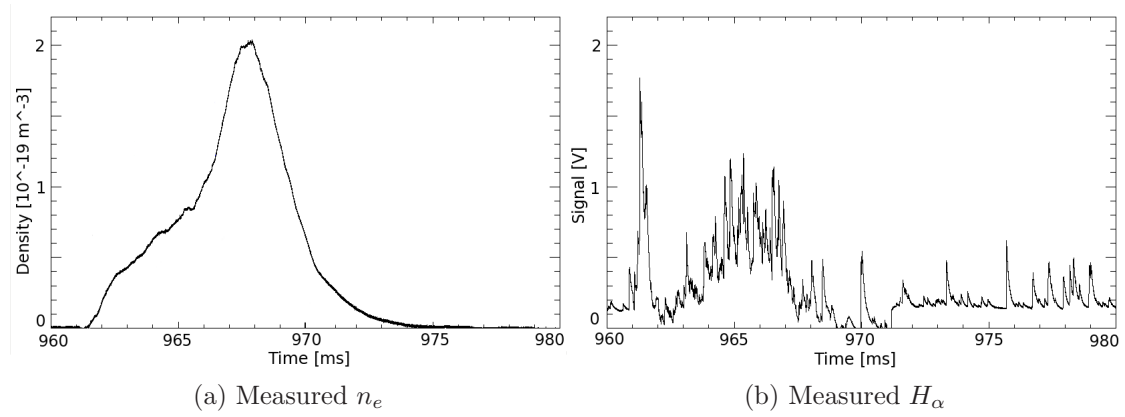


Figure 6.1: COMPASS's shot 1519

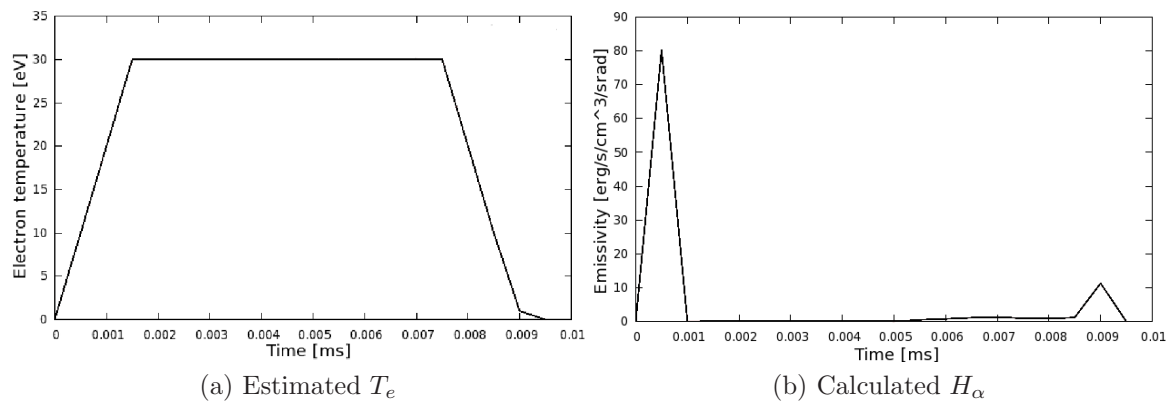


Figure 6.2: FLYCHK simulation for 1519 shot with offset 961 ms

peak densities. Both peaks are easily recognizable in simulation, however the second peak is hardly recognizable in measured H_α .

There are many differences between real H_α and the modelled one, which is caused by the CR model inaccuracy and numerical limitations. However, such differences were expected.

Chapter 7

Conclusion

New diagnostic has been developed in order to measure plasma radiation in visible range. The diagnostic consists of two parts: the multichannel diagnostic and few spectrometers. Few photomultiplier tubes can provide an additional data. Important plasma parameters will be estimated in cooperation with other diagnostic: impurity inflows, recycling processes, particle confinement estimations, MHD activity or effective ionic charge.

Many calibrations and check measurements were needed during the development. The multichannel system calibrations (of detector sensitivity, alignment and amplifier's time constant) were done. Results of multichannel calibrations proved that developing of the multichannel diagnostic were successful. The spectrometers calibrations were done. The calibration of first spectrometer at lower wavelength was successful, the second one was not successful due to unsuitable light source with few spectral lines in range of interest only. Finally two photomultiplier tubes were tested too. A simulation of plasma electron temperature during tokamak shot was done.

The diagnostic should be operational until the end of 2011.

Bibliography

- [1] NAYDENKOVA, Diana et al. Design of New Optical System for Visible Plasma Radiation Measurements at COMPASS Tokamak. In *WDS' 08 Proceedings of Contributed Papers: Part II - Physics* J. Safrankova and J. Pavlu. Prague: MATFYZPRESS, 2008. P.100-104. ISBN 978-80-7378-066-1.
- [2] NAYDENKOVA, Diana et al. The Optical System for Visible Plasma Radiation Measurements in the COMPASS Tokamak – Design and Testing. In *Acta Technica*. I. Dolezal. Prague: Institute of Thermomechanics ASCR, Volume 56, 2011. Will be published.
- [3] NAYDENKOVA, Diana et al. First spectroscopic measurements on the COMPASS tokamak. In *WDS'09 Proceedings of Contributed Papers: Part II - Physics of Plasmas and Ionized Media*. J. Safrankova, J. Pavlu. Prague: MATFYZPRESS, 2009. P. 158-162. ISBN 978-80-7378-102-6.
- [4] ŠESTÁK, D. et at. Design and engineering of optical diagnostic for COMPASS. In *Fusion Engineering and Design 84*. Elsevier, 2009. P. 1755-1758.
- [5] NAYDENKOVA, Diana et al. Progress in Multi channel Optical System for Visible Plasma Radiation Measurement at COMPASS Tokamak. In *WDS'10 Proceedings of Contributed Papers: Part II - Physics of Plasmas and Ionized Media*. J. Safrankova, J. Pavlu. Prague: MATFYZPRESS, 2010. P. 18–21. ISBN 978-80-7378-140-8
- [6] TKACHENKO, Nikolai V. *Optical Spectroscopy: Methods and Instrumentations*, First edition. Elsevier, 2006. ISBN 978-0-444-52126-2
- [7] KUNZE, Hanz-Joachim. *Introduction to Plasma Spectroscopy*. 1th edition. Springer, 2009. ISBN 978-3-642-02232-6
- [8] OCEAN OPTICS, *HR2000+ High-speed Fiber Optic Spectrometer: Installation and Operational Manual Document Number 294-00000-000-02-0208*[online]. ©2010, [cit. 2011-06-22]. URL: <<http://www.oceanoptics.com/technical/hr2000+.pdf>>
- [9] VLČEK Jiří, WEINZETTL Vladimír. *Předzesilovač k detektoru záření*, [cit. 2010-06-05]. Institute of Plasma Physics, AVČR. vlcek@ipp.cas.cz, vwei@ipp.cas.cz. Not-published.
- [10] HAMAMATSU PHOTONICS, *Si photodiode array: S4111/S4114 series* [online]. ©2008, [cit. 2011-06-22]. URL: <http://sales.hamamatsu.com/assets/pdf/parts_S/s4111-16q_etc_kmpd1002e06.pdf>
- [11] THE MATHWORKS, INC. *regress.m* [file]. ©1993-2005, Version 2.13.2.7. last revision 18.11.2005 14:29:01 [cit. 2011-06-22]. URL:<[\\$MATLABPATH/R2008b/toolbox/stats/regress.m](#)>

- [12] OCEAN OPTICS, *Calibration Light Source CAL-2000: Installation and Operational Manual Document Number 000-10000-010-02-1209* [online]. 2009, [cit. 2011-06-22]. URL: <<http://www.oceanoptics.com/technical/cal2000.pdf>>
- [13] BUR. INTL. POIDS ET MESURES, *Le Système international d'Unités = The international System of Units*. 8e édition. France. 2006. ISBN 92-822-2213-6
- [14] WESSON, J., et al. *Tokamaks*. 3rd edition. Clarendon: Press-Oxford, 2004. ISBN 0-19-8509227.
- [15] VAN HOEY, Olivier. *Visible light measurements on the COMPASS tokamak*. 2010. Diploma thesis at Faculty of Engineering of University Gent in Department of Applied Physics. Promoter of the diploma thesis Prof. Dr. Ir. G. Van Oost
- [16] ITT VISUAL INFORMATION SOLUTIONS, *Getting Started with IDL* [online] . ©November 2007, [cit. 2011-06-21]. URL:<<http://www.astro.virginia.edu/class/oconnell/ast511/IDLresources/getting-started-IDL-v7.0.pdf>>
- [17] LEE, Richard W. *The How to For FLY* [online]. ©1995. last revision November 1995 [cit. 2011-06-22]. URL: <<http://nlte.nist.gov/FLY/Doc/FLY95.pdf>>
- [18] CHUNG, H.K. et al. *The How To For FLYCHK@NIST* [online]. ©2008. last revision November 2008 [cit. 2011-06-22], URL: <http://nlte.nist.gov/FLY/Doc/Manual_FLYCHK_Nov08.pdf>
- [19] WIKIBOOKS. *LATEX* [online]. ©2005-2008, last revision 5th of November 2008. URL: <<http://upload.wikimedia.org/wikipedia/commons/2/2d/LaTeX.pdf>>
- [20] BOLDIŠ, Petr. *Bibliografické citace dokumentů podle ČSN ISO 690 a ČSN ISO 690-2: Část 1 - Citace: metodika a obecná pravidla*. Version 3.3 (2004). ©1999-2004, last revision 11. 11. 2004. URL:<<http://www.boldis.cz/citace/citace1.pdf>>
- [21] BOLDIŠ, Petr. *Bibliografické citace dokumentů podle ČSN ISO 690 a ČSN ISO 690-2: Část 2 - Modely a příklady citací u jednotlivých typů dokumentů*. Version 3.0 (2004) ©1999-2004, last revision 11. 11. 2004. URL:<<http://www.boldis.cz/citace/citace2.pdf>>